energies

Article

Improving Efficiency of a Pole-Changing Vernier Machine Considering Residual Magnetic Flux Density

Sung-Hyun Lee, Jung-Woo Kwon and Byung-Il Kwon *

Department of Electrical and Electronic Engineering, Hanyang University, Ansan 15588, Republic of Korea; tjdgus9417@hanyang.ac.kr (S.-H.L.); jwkonwis@hanyang.ac.kr (J.-W.K.)
* Correspondence: bikwon@hanyang.ac.kr; Tel.: +82-31-400-5165

Abstract: This paper presents the efficiency improvement of a pole-changing vernier machine (PCVM) by considering the residual magnetic flux density (B_r) of low coercivity force (LCF) permanent magnets (PMs). The PCVM operates in two modes: vernier machine (VM) mode and permanent magnet synchronous machine (PMSM) mode, achieved through pole-changing. Pole-changing involves reversing the magnetic flux direction of LCF PM to alter the number of rotor pole pairs. By changing the number of rotor pole pairs, the PCVM operates as a VM mode at low speeds, providing high torque, and as a PMSM mode at high speeds, offering high efficiency. To achieve this, a combination of high coercivity force (HCF) PM and LCF PM is utilized in a single structure. The magnetic flux direction in the LCF PM is determined by B_r, and the highest efficiency is achieved when B_r reaches its maximum value $|B_{rm}|$. This paper focuses on improving efficiency by obtaining B_{rm} in VM mode and $-B_{rm}$ in PMSM mode through the design process. Additionally, finite element analysis (FEA) is employed to compare the performance of the improved model, which considers B_r, with that of the conventional model, designed without considering B_r. The improved model achieves higher B_r values in each mode compared to the conventional model, resulting in increased torque density. Consequently, this leads to improved efficiency.

Keywords: efficiency improvement; pole-changing; residual magnetic flux density; vernier machine; permanent magnet synchronous machine

check for updates

Citation: Lee, S.-H.; Kwon, J.-W.; Kwon, B.-I. Improving Efficiency of a Pole-Changing Vernier Machine Considering Residual Magnetic Flux Density. *Energies* **2023**, *16*, 6707. https://doi.org/10.3390/en16186707

Academic Editor: Terence O'Donnell

Received: 18 August 2023
Revised: 12 September 2023
Accepted: 18 September 2023
Published: 19 September 2023

1. Introduction

Permanent magnet synchronous machines (PMSMs) have gained significant attention due to their high torque density and efficiency [1–3]. However, the constant airgap flux of permanent magnets (PMs) presents a challenge for the operation of the machine over a wide speed range [4]. Designing a machine solely for low-speed operation results in decreased efficiency at higher speeds due to high iron losses. Conversely, optimizing for high-speed operation leads to lower efficiency and torque at low speeds as the magnetic flux density decreases due to high copper losses [5,6].

Vernier machines (VMs) have emerged as a viable option for low-speed, high-torque applications like wind turbines. VMs offer a magnetic gear effect that provides high torque density and efficiency at low speeds [7–9]. The VM generates a back electromotive force (B−EMF) approximately 1.5–3 times larger than that of a typical PMSM, resulting in substantial torque even at low speeds. As a result, VMs allow for compact size and high efficiency in the low-speed range [10–13]. However, VMs typically have a higher number of pole pairs compared to conventional PMSMs, resulting in increased core losses. These losses escalate as the speed rises, leading to decreased efficiency at high speeds. Consequently, VMs have primarily been studied and optimized for low-speed applications, limiting their advantages [14,15].

Efforts have been made to apply the concept of pole-changing, based on the memory machine principle [16–19], to VMs to combine the advantages of high torque at low speeds from VMs and high efficiency at high speeds from PMSMs within a single machine structure [20–23]. One such development is the pole-changing vernier machine (PCVM) [20], where pole-changing is achieved by utilizing both low coercivity force (LCF) and high coercivity force (HCF) PMs on the rotor. By reversing the magnetic flux direction of the LCF PM, the number of rotor poles can be altered, enabling the PCVM to operate as a VM at low speeds, providing high torque, and as a PMSM at high speeds, offering high efficiency. Consequently, the PCVM exhibits high efficiency across a wide speed range. A PCVM with high efficiency across a wide speed range can offer significant advantages in applications with wide speed ranges and multiple loads, such as washing machines and electric vehicles (EVs) [24–26].

However, previous studies [20] focused primarily on proposing the pole-changing topology under the ideal assumption that the residual magnetic flux density (B_r) of the LCF PM would reach its maximum value, $|B_{rm}|$. Consequently, the efficiency of the conventional PCVM model, designed without considering B_r of the LCF PM, decreased across the wide speed range due to low magnetic flux density when B_r of the LCF PM failed to attain B_{rm} or $-B_{rm}$ in each mode.

This paper aims to enhance the efficiency of the PCVM by improving the magnetic flux density through design considerations for B_r of the LCF PM. Section 2 presents an overview of the PCVM structure, the operating principles of its two modes achieved through pole-changing, and the pole-changing process based on variations in B_r of the LCF PM. Section 3 selects the design parameters for the PCVM, considering B_r of the LCF PM, and determines the range of these parameters. The final values of the design parameters are obtained through the pole-changing process within the established range. In Section 4, the improved model is validated to achieve B_{rm} in VM mode and $-B_{rm}$ in PMSM mode. The efficiency improvement is then verified by comparing the performance of the improved model, designed with consideration of B_r of the LCF PM, with that of the conventional model, designed without such consideration. Finally, Section 5 concludes the paper.

2. Operating Principle and Pole-Changing Process

2.1. Structure of PCVM

The PCVM structure, as depicted in Figure 1, comprises 36 slots with concentrated three-phase armature windings in the stator slots. To achieve pole-changing, two types of PMs with different coercivities, namely HCF PMs and LCF PMs, are utilized. In the consequent pole structure, half of the HCF PMs and LCF PMs are replaced with an iron pole [27]. Pole-changing is accomplished by reversing the magnetic flux direction of the LCF PM, thereby altering the number of rotor pole pairs.

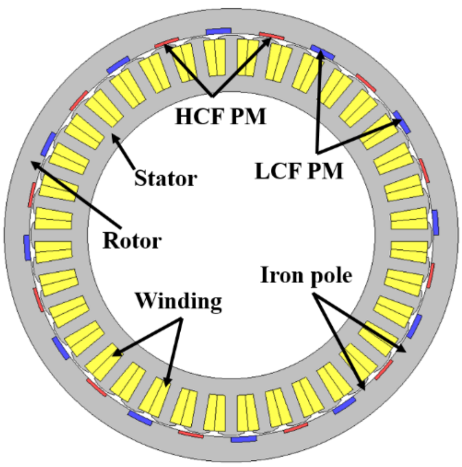

Figure 1. Structure of PCVM.

2.2. Operating Principle of Two Modes

Figure 2 shows the 12-segment structure of PCVM and indicates the magnetic flux direction of PMs with arrows.

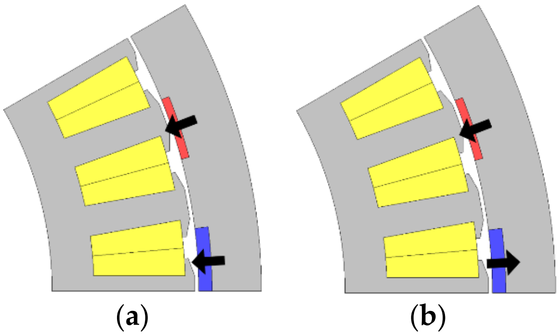

Figure 2. Magnetic flux direction of PMs: (**a**) VM mode; (**b**) PMSM mode.

The VM mode operates based on the principle described in Equation (1), which utilizes the magnetic gear effect.

$$Z_r = Z_s \pm p \tag{1}$$

Here, Z_r represents the number of rotor pole pairs, Z_s is the number of stator slots, and p denotes the number of armature winding pole pairs. As shown in Figure 2a, the PCVM operates in VM mode when the magnetic flux direction of HCF PM and LCF PM is the same. This condition is achieved by satisfying Equation (1) with Z_s = 36, Z_r = 24, and p = 12.

The PMSM mode operates based on the principle described by Equation (2), where torque is generated through the interaction between rotor pole pairs and armature winding pole pairs.

$$Z_r = p \tag{2}$$

As depicted in Figure 2b, the PCVM operates in PMSM mode when the magnetic flux directions of the HCF PM and LCF PM are different. This condition is achieved by satisfying Equation (2) with Z_r = 12, p = 12, due to the pole-changing that results in a different direction of the LCF PMs.

2.3. Pole-Changing Process Using B_r of the LCF PM

Figure 3 illustrates the flowchart of the pole-changing process using B_r of the LCF PM, while Figure 4 represents the B−H curve of the LCF PM. The process begins by applying a current pulse for magnetization to obtain a positive value of B_r in the LCF PM. Furthermore, B_r of the LCF PM changes according to the magnetization process, as indicated by the green line on the B−H curve in Figure 4. The B_r value is calculated using finite element analysis (FEA). If B_r falls within the range of "$0 < B_r \leq B_{rm}$", the PCVM operates in VM mode, as depicted in Figure 2a. If B_r is not within the specified range, the magnetization process is repeated by returning to the application of current pulses for magnetization, as indicated in the flowchart in Figure 3.

Next, a current pulse is applied for demagnetization to obtain a negative value of B_r in the LCF PM. B_r of the LCF PM changes according to the demagnetization process, represented by the orange line on the B−H curve in Figure 4. The B_r value is calculated using FEA. If B_r falls within the range of "$-B_{rm} \leq B_r < 0$", the PCVM operates in PMSM mode, as shown in Figure 2b. If B_r is not within the specified range, the demagnetization process is repeated by returning to the application of current pulses for demagnetization, following the flowchart in Figure 3.

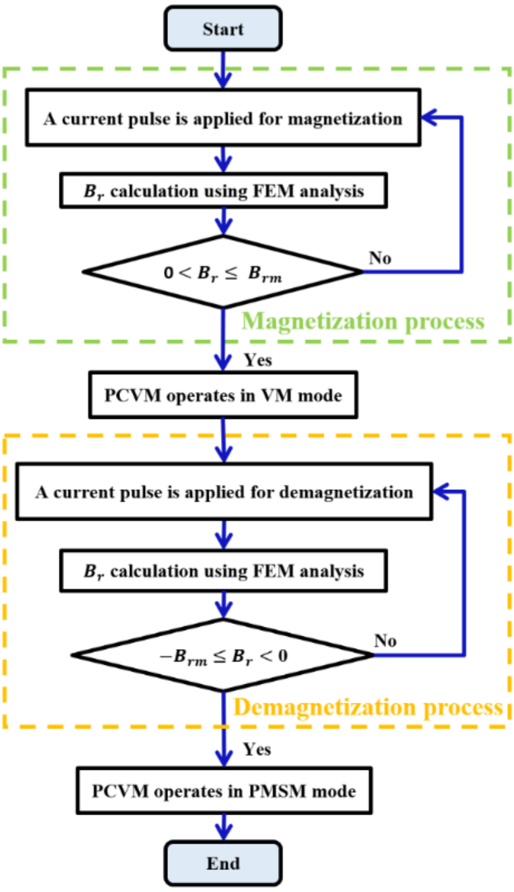

Figure 3. Flowchart of the pole-changing process.

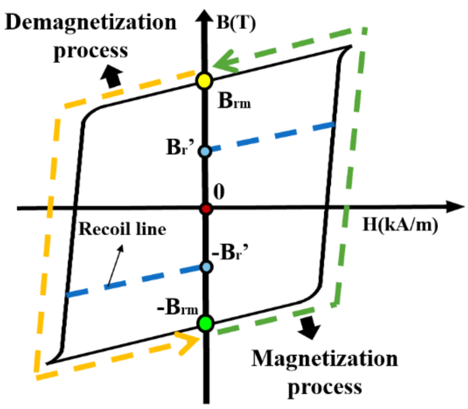

Figure 4. B−H curve of LCF PM.

3. Design That Considers B_r of the LCF PM

3.1. Conventional Model without Considering B_r

The conventional model focused primarily on proposing a pole-changing topology, assuming an ideal condition where all areas of the LCF PM exhibit either B_{rm} or $-B_{rm}$, as shown by the B−H curve in Figure 4. However, this design overlooked the B_r of the LCF PM, resulting in reduced efficiency due to lower torque density when the B_r of LCF PMs fell along the recoil line, such as B_r' or $-B_r'$ in Figure 4. The specifications of the conventional model, designed without considering B_r of the LCF PM, are summarized in Table 1.

Table 1. Design specifications of conventional model.

Item	Unit	Value
Rotor outer diameter	mm	300
Stator outer diameter	mm	265
Air gap length	mm	1
Number of slots	--	36
Rotor pole pairs (VM mode)	--	24
Rotor pole pairs (PMSM mode)	--	12
HCF/LCF PM coercivity	kA/m	650/318
HCF/LCF PM remanence	T	0.87/0.7

3.2. Selection and Range of Design Parameters

Designing with consideration of the B_r of LCF PM during the pole-changing process can improve efficiency by achieving B_{rm} in VM mode and $-B_{rm}$ in PMSM mode. As seen in Figure 3, a current pulse is applied to achieve $|B_{rm}|$. However, the magnitude of the current pulses is limited by the inverter capacity. For the research objective of high efficiency over a wide speed range in applications such as washing machines and EVs, an inverter capacity of 55 kW was adopted in this study. The magnitude of the current pulses is <100 A due to current limitations imposed by the inverter capacity.

To obtain B_{rm} or $-B_{rm}$ within the limited magnitude of the current pulse, specific design parameters were chosen, and their ranges were determined. These design parameters were identified based on previous research [28], which investigated the impact of design parameter variations on the current pulse magnitude. The selected design parameters include stator tooth width, LCF PM width, and LCF PM height. The stator tooth width governs the flux path for current pulse magnetization and demagnetization, while the LCF PM width and height correspond to the regions where these processes occur. Consequently, increasing the stator tooth width and decreasing the LCF PM width and height lead to a reduction in the current pulse magnitude [28,29].

Figure 5 depicts the magnitude of the current pulse with variations in the design parameters. Feasible ranges for the design parameters were determined as shown on the x-axis in Figure 5a–c, considering manufacturing constraints, slot fill factor, and prevention of PM scattering. In Figure 5, the effect of a single design parameter on the current pulse magnitude is examined while keeping the other design parameters constant. For example, in Figure 5a, when the stator tooth width changes, the LCF PM width and height remain constant. The values at which the design parameters are kept constant are as follows: The stator tooth width is set to its maximum value of 10 mm, while the LCF PM width and height are set to their minimum values of 12 and 2 mm, respectively. These settings are chosen to minimize the current pulse magnitude, as explained earlier. Furthermore, since magnetization current pulses are typically larger than demagnetization pulses [30], the current pulses shown on the y-axis in Figure 5 represent the magnitude of the magnetization current pulse.

As a result, the range of the design parameters is determined based on a maximum current pulse magnitude of 100 A due to current limitations imposed by the inverter capacity. In Figure 5, a current pulse size of 100A has been represented by a red dashed line to indicate the limitation on current pulse magnitude. Additionally, current pulse magnitudes based on design parameters are depicted as blue dots. In Figure 5a, the design parameter range for the stator tooth width is determined as 8–10 mm, with the condition that the magnitude of the current pulses is less than 100 A. In Figure 5b, the design parameter range for the LCF PM width is determined as 12–18 mm, with the condition that the magnitude of the current pulses is less than 100 A. Additionally, in Figure 5c, the design parameter range for the LCF PM height is determined as 2–4 mm, with the condition that the magnitude of the current pulses is less than 100 A.

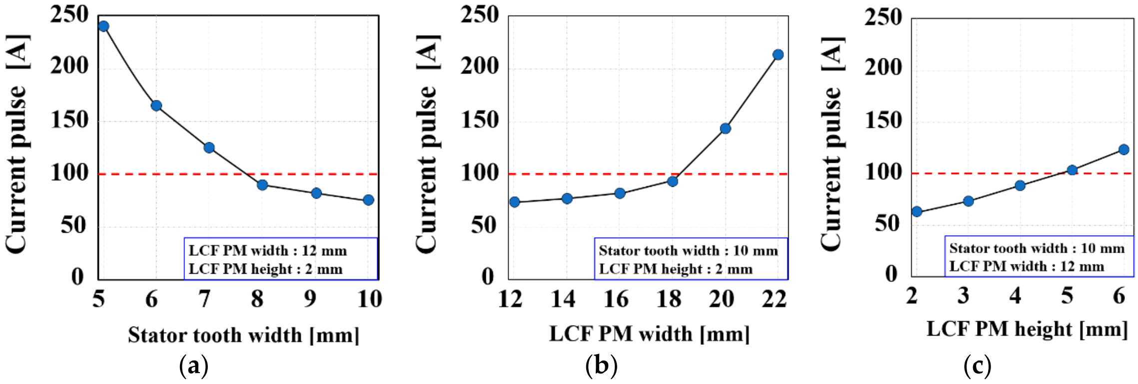

Figure 5. Magnitude of current pulse with variation in (**a**) stator tooth width, (**b**) LCF PM width, and (**c**) LCF PM height.

3.3. Determining the Final Values of Design Parameters

Figure 6 depicts a flowchart illustrating the process of determining the final values of the design parameters according to the pole-changing process and the range of the design parameters. In this process, as described in Section 2, the magnitude of the current pulses is limited, and the objective has been modified from achieving B_r to B_{rm} for efficiency improvement.

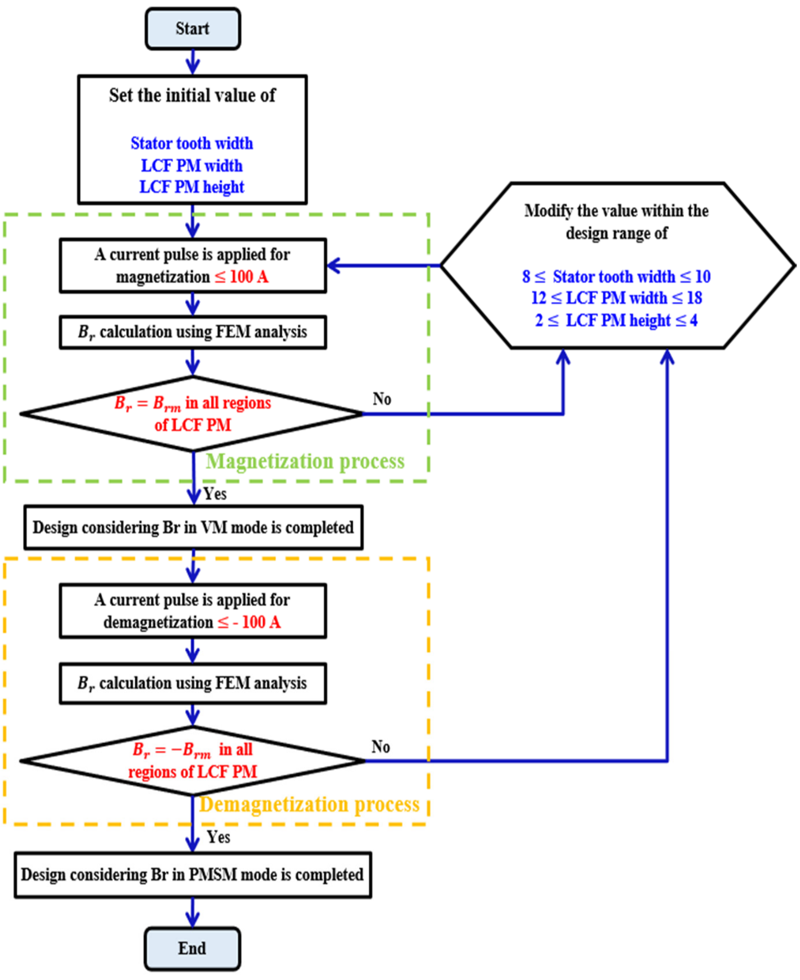

Figure 6. Flowchart for determining the final values of design parameters according to the pole-changing process and the range of the design parameters.

The flowchart is explained in three parts: the magnetization process, the demagnetization process, and the determination of the final values of design parameters. Initially, the minimum value from the range of each design parameter is selected as the initial value. The stator tooth width is set to 8 mm, the LCF PM width is set to 12 mm, and the LCF PM height is set to 2 mm. Subsequently, the magnetization process is performed by applying a current pulse limited to 100 A. If any region of the LCF PM fails to achieve B_{rm}, the values of the design parameters within their respective ranges are adjusted, and the magnetization process is repeated. Next, the demagnetization process is conducted by applying a current pulse limited to -100 A. If any region of the LCF PM fails to attain $-B_{rm}$, the values of the design parameters are modified again within their respective ranges, and the magnetization process is repeated. Finally, a combination of design parameter values that satisfies both the magnetization and demagnetization processes is derived. The combination of design parameter values that achieves the highest efficiency in each mode is selected from the derived combinations. In this manner, the design for the VM and PMSM modes with the highest efficiency is completed in the PCVM. This design, considering B_r, improves the efficiency of each mode, enabling high efficiency over a wide speed range.

The final values of the design parameters for the conventional and improved models are summarized in Table 2.

Table 2. Final values of the design parameters.

Parameter	Unit	Conventional	Improved
Stator tooth width	mm	7	9
LCF PM width	mm	17	16
LCF PM height	mm	5	4

4. Performance Evaluation

4.1. Confirmation of B_{rm} with the Pole-Changing Process

To confirm that B_r of the improved model's LCF PM obtains B_{rm} in VM mode and $-B_{rm}$ in PMSM mode, FEA was performed using JMAG Version 22 to apply a current pulse of the pole-changing process and calculate B_r in each mode. It has been verified in numerous studies [31,32] that the commercial software JMAG provides values that are highly consistent with experimental results.

The LCF PMs are located as indicated in Figure 7a. Furthermore, a current pulse is applied to magnetize the LCF PMs in the opposite direction, resulting in a change in the magnetic flux direction of all LCF PMs. The B_r value of the LCF PM changes along the magnetization process, as shown by the green line on the B−H curve in Figure 4, where its value is "$0 < B_r \leq B_{rm}$". Consequently, as shown in Figure 7b, the machine operates in VM mode. The LCF PMs move at a mechanical angle of 15° and then are fixed, as shown in Figure 7c. Moreover, a current pulse is applied for demagnetization in the opposite direction to the magnetization of the LCF PMs, changing the Then, a current pulse is applied for demagnetization in the opposite direction to the magnetic flux direction of the LCF PMs. The B_r value of the LCF PM changes along the demagnetization process, as shown by the orange line on the B−H curve in Figure 4, where its value is "$-B_{rm} \leq B_r < 0$". Therefore, as shown in Figure 7d, the machine operates in PMSM mode.

As shown in Figure 7a,c, a magnetic field of approximately 0.7 T affects all regions of the LCF PM in the magnetic flux density distribution. Therefore, it was confirmed that the design considering B_r for efficiency improvement was completed since the LCF PM has B_{rm} in the VM mode and $-B_{rm}$ in the PMSM mode. Furthermore, it can be confirmed that the magnetic flux direction of the LCF PMs has changed by observing the alteration of the flux lines depicted in Figure 7b,d. Therefore, the number of rotor pole pairs changes, confirming that pole-changing is complete.

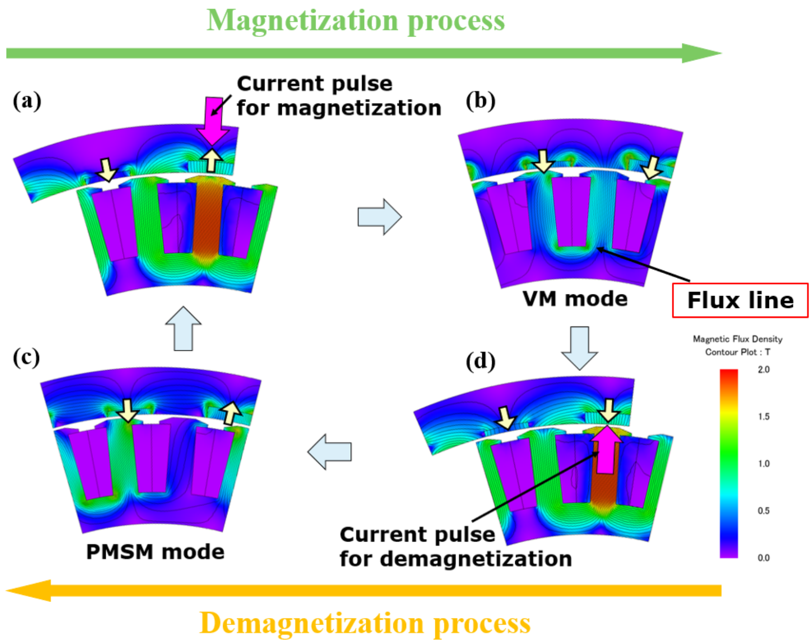

Figure 7. Magnetic flux density distribution and flux line according to the pole-changing process of the improved model: (**a**) PMSM mode to VM mode; (**b**) VM mode; (**c**) VM mode to PMSM mode; and (**d**) PMSM mode.

4.2. Comparison of Performances

The performance of the improved model designed considering the B_r of LCF PM was compared with the conventional model designed without considering the B_r of LCF PM. The B−EMF comparison of the conventional and improved models of the PCVM during VM and PMSM modes is shown in Figure 8. Figure 8a shows that B−EMF in VM mode is 51.6 V_{rms} in the conventional model and 77.5 V_{rms} in the improved model. Figure 8b shows that B−EMF in PMSM mode is 40.7 V_{rms} in the conventional model and 58.3 V_{rms} in the improved model. Therefore, the B−EMF of each mode was improved by design, considering the B_r of LCF PM.

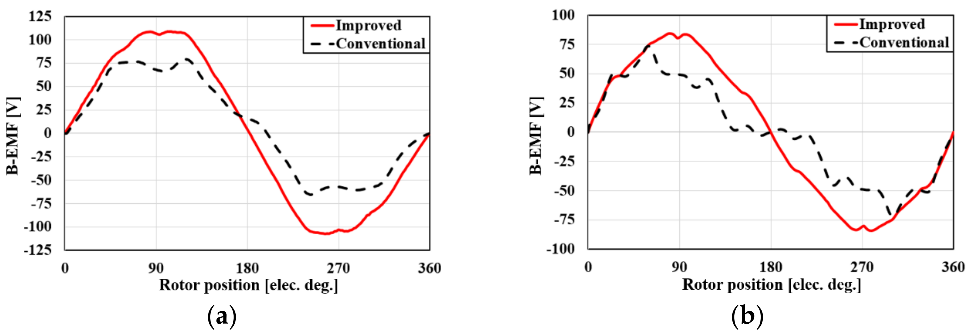

Figure 8. Comparison of the B−EMF of the conventional model and the improved model: (**a**) VM mode and (**b**) PMSM mode.

The output torque comparison of the conventional and improved models of the PCVM during VM and PMSM modes is shown in Figure 9. Figure 9a shows that the torque in VM mode is 12.7 Nm in the conventional model and 21.8 Nm in the improved model. Figure 9b shows that the torque in PMSM mode is 10.5 Nm in the conventional model and 16.4 Nm in the improved model. Therefore, the torque of each mode was improved by design, considering the B_r of LCF PM.

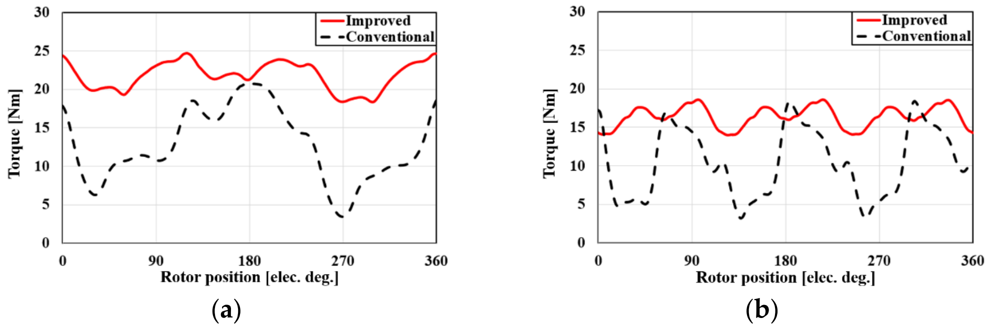

Figure 9. Comparison of the output torque of the conventional model and the improved model: (**a**) VM mode and (**b**) PMSM mode.

To compare the magnetic flux density distribution in the VM mode of the improved model shown in Figure 7b with the conventional model, it is presented in Figure 10. Figure 10a shows that the LCF PM could not obtain B_{rm} because the design considering the B_r of LCF PM was not performed. Figure 10b shows that the LCF PM has a high magnetic flux density by obtaining a B_{rm} because the design considering the B_r of LCF PM was performed.

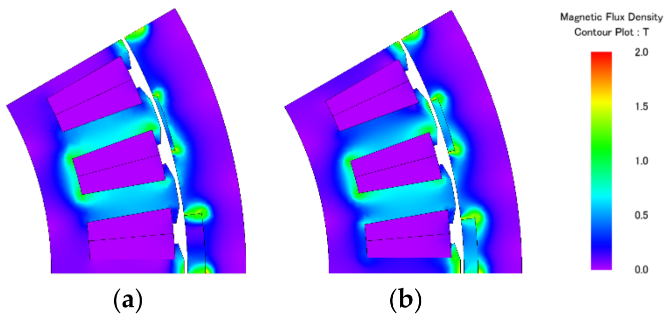

Figure 10. Comparison of the magnetic flux density distribution of the VM mode: (**a**) conventional model and (**b**) improved model.

To compare the magnetic flux density distribution in the PMSM mode of the improved model shown in Figure 7d with the conventional model, it is presented in Figure 11. Figure 11a shows that the LCF PM could not obtain a $-B_{rm}$ because the design considering the B_r of LCF PM was not performed. Figure 11b shows that the LCF PM has a high magnetic flux density by obtaining a $-B_{rm}$ because the design considering the B_r of LCF PM was performed.

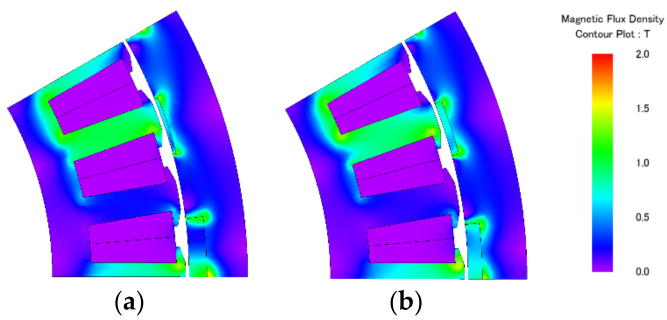

Figure 11. Comparison of the magnetic flux density distribution of the PMSM mode: (**a**) conventional model and (**b**) improved model.

To confirm the efficiency improvement through the design, considering the B_r of LCF PM, the efficiency of each mode is calculated. The efficiency is calculated using Equation (3).

$$\eta = \frac{P_{out}}{P_{out} + P_c + P_i} \times 100\% \tag{3}$$

where P_{out}, P_c , and P_i are the output power, copper loss, and iron loss, respectively. The efficiency of the VM mode calculated using Equation (3) is 86.9% for the conventional model and 90.7% for the improved model. Furthermore, the PMSM mode is 92.5% for the conventional model and 94.9% for the improved model.

Table 3 presents a performance comparison of the conventional and improved models. As shown in Figures 8 and 9, it is observed that the improved model for each mode shows enhanced performance compared to the conventional model under the same operating conditions. The improved model achieved higher torque density by obtaining B_{rm} in the VM mode and $-B_{rm}$ in the PMSM mode, considering the design with B_r. Moreover, when operating in PMSM mode, the number of rotor pole pairs is reduced by half compared to VM mode due to pole-changing. This reduction in pole pairs leads to a decrease in iron losses, thereby enhancing efficiency at high speeds. The improved model and the conventional model have the same current conditions, so they have the same copper losses. In the improved model, as a result of considering B_r in the design process, there was a slight increase in iron losses due to the increase in stator tooth width compared to the conventional model. Nevertheless, the substantial increase in B_r significantly enhances torque density. Therefore, the efficiency of the improved model is enhanced by having a high magnetic flux density in each mode as the design considering the B_r of LCF PM is performed.

Table 3. Performance comparison of conventional and improved model.

Item	Unit	Conventional		Improved	
Machine mode	--	VM	PMSM	VM	PMSM
Speed	rpm		300		
B−EMF	V	51.6	40.8	77.5	58.3
Terminal voltage	V	104.2	65.6	141.4	86.8
Average torque	Nm	12.7	10.5	21.8	16.4
Copper loss	W	6.9	6.9	6.9	6.9
Iron loss	W	53.4	19.8	62.9	20.7
Efficiency	%	86.9	92.5	90.7	94.9

5. Conclusions

In this study, a design considering the B_r of LCF PMs was used to improve the efficiency of the PCVM. To verify the efficiency improvement, the efficiencies of the improved model, designed considering the B_r of the LCF PM, and the conventional model, designed without considering the B_r of the LCF PM, were compared in each mode. In VM mode, the efficiency of the conventional model was 86.9%, while the efficiency of the improved model was 90.7%. This represents a 3.8% increase in efficiency compared to the conventional model. In PMSM mode, the efficiency of the conventional model was 92.5%, while that of the improved model was 94.9%. This corresponds to a 2.4% increase in efficiency compared to the conventional model.

The improved model, in the design process that considered B_r, resulted in a slight increase in iron losses compared to the conventional model due to the increase in the stator tooth width. However, the substantial increase in B_r significantly enhances torque density. The improved model increased torque density by obtaining B_{rm} in VM mode and $-B_{rm}$ in PMSM mode through the design considering B_r. When operating in PMSM mode, the number of rotor pole pairs is reduced by half compared to VM mode due to pole-changing. This reduction in pole pairs decreases the frequency at high speeds, resulting in reduced iron losses and further enhancing efficiency. Therefore, PCVM achieved high torque in

VM mode at low speeds and high efficiency in PMSM mode at high speeds, owing to the design considerations of LCF PM's B_r. This improved efficiency across a wide speed range.

PCVM has been proposed previously, but research on this relatively new structure has not been extensively conducted. This study has contributed to improving the efficiency of PCVM by carefully considering the characteristics of LCF PM. PCVM used only two operating points: low speed and high speed. Future research can expand into applications that utilize multiple loads in wide speed ranges, similar to EVs, allowing for performance improvement.

Author Contributions: S.-H.L. conceived the initial idea, performed the model design, analyzed the data, and wrote this paper; J.-W.K. analyzed the model and assisted with English correction; B.-I.K. supervised the overall research. All authors have read and agreed to the published version of the manuscript.

Funding: This work was supported by the National Research Foundation of Korea (NRF) grant funded by the Korean government (MSIT) (No. NRF-2020R1A2B5B01002400).

Data Availability Statement: The data that support the findings of this study are available on request from the corresponding author, B.-I.K., upon reasonable request.

Conflicts of Interest: The authors declare no conflict of interest.

References

1. Fang, L.; Jung, J.W.; Hong, J.P.; Lee, J.H. Study on High-Efficiency Performance in Interior Permanent-Magnet Synchronous Motor with Double-Layer PM Design. *IEEE Trans. Magn.* **2008**, *44*, 4393–4396. [CrossRef]
2. Ba, X.; Gong, Z.; Guo, Y.; Zhang, C.; Zhu, J. Development of Equivalent Circuit Models of Permanent Magnet Synchronous Motors Considering Core Loss. *Energies* **2022**, *15*, 1995. [CrossRef]
3. Hou, L.; Ma, J.; Wang, W. Sliding Mode Predictive Current Control of Permanent Magnet Synchronous Motor with Cascaded Variable Rate Sliding Mode Speed Controller. *IEEE Access* **2022**, *10*, 33992–34002. [CrossRef]
4. Tapia, J.; Leonardi, F.; Lipo, T. Consequent-pole permanent-magnet machine with extended field-weakening capability. *IEEE Trans. Ind. Appl.* **2003**, *39*, 1704–1709. [CrossRef]
5. Kwon, J.-W.; Kwon, B.-I. High-Efficiency Dual Output Stator-PM Machine for the Two-Mode Operation of Washing Machines. *IEEE Trans. Energy Convers.* **2018**, *33*, 2050–2059. [CrossRef]
6. Baloch, N.; Kwon, J.-W.; Ayub, M.; Kwon, B.-I. Low-Cost Dual-Mechanical-Port Dual-Excitation Machine for Washing Machine Application. *IEEE Access* **2019**, *7*, 87141–87149. [CrossRef]
7. Toba, A.; Lipo, T.A. Generic torque-maximizing design methodology of surface permanent-magnet vernier machine. *IEEE Trans. Ind. Appl.* **2000**, *36*, 1539–1546. [CrossRef]
8. Kim, B.; Lipo, T.A. Analysis of a PM Vernier Motor with Spoke Structure. *IEEE Trans. Ind. Appl.* **2015**, *52*, 217–225. [CrossRef]
9. Kim, B. Characteristic analysis of a vernier PM motor considering adjustable speed control. In Proceedings of the 2016 IEEE Transportation Electrification Conference and Expo, Asia-Pacific (ITEC Asia-Pacific), Busan, Republic of Korea, 1–4 June 2016; pp. 671–676. [CrossRef]
10. Zou, T.; Li, D.; Qu, R.; Jiang, D.; Li, J. Advanced High Torque Density PM Vernier Machine with Multiple Working Harmonics. *IEEE Trans. Ind. Appl.* **2017**, *53*, 5295–5304. [CrossRef]
11. Du, K.; Xu, L.; Zhao, W.; Liu, G. Analysis and Design of a Fault-Tolerant Permanent Magnet Vernier Machine with Improved Power Factor. *IEEE Trans. Ind. Electron.* **2021**, *69*, 4353–4363. [CrossRef]
12. Zhao, W.; Sun, X.; Ji, J.; Liu, G. Design and Analysis of New Vernier Permanent-Magnet Machine with Improved Torque Capability. *IEEE Trans. Appl. Supercond.* **2016**, *26*, 1–5. [CrossRef]
13. Xu, L.; Zhao, W.; Liu, G.; Song, C. Design Optimization of a Spoke-Type Permanent-Magnet Vernier Machine for Torque Density and Power Factor Improvement. *IEEE Trans. Veh. Technol.* **2019**, *68*, 3446–3456. [CrossRef]
14. Wang, H.; Fang, S.; Yang, H.; Lin, H.; Li, Y.; Qin, L.; Zhou, Y. Loss Calculation and Temperature Field Analysis of Consequent-Pole Hybrid Excited Vernier Machine. *IEEE Trans. Magn.* **2017**, *53*, 1–5. [CrossRef]
15. Zhao, F.; Kim, M.-S.; Kwon, B.-I.; Baek, J.-H. A Small Axial-Flux Vernier Machine with Ring-Type Magnets for the Auto-Focusing Lens Drive System. *IEEE Trans. Magn.* **2016**, *52*, 1–4. [CrossRef]
16. Ostovic, V. Memory motors-a new class of controllable flux PM machines for a true wide speed operation. In Proceedings of the Conference Record of the 2001 IEEE Industry Applications Conference. 36th IAS Annual Meeting (Cat. No.01CH37248), Chicago, IL, USA, 30 September–4 October 2002; Volume 4, pp. 2577–2584. [CrossRef]
17. Ostovic, V. Pole-changing permanent-magnet machines. *IEEE Trans. Ind. Appl.* **2002**, *38*, 1493–1499. [CrossRef]
18. Yang, H.; Zhu, Z.Q.; Lin, H.; Wu, D.; Hua, H.; Fang, S.; Huang, Y.-K. Novel High-Performance Switched Flux Hybrid Magnet Memory Machines with Reduced Rare-Earth Magnets. *IEEE Trans. Ind. Appl.* **2016**, *52*, 3901–3915. [CrossRef]

19. Yang, H.; Zheng, H.; Lin, H.; Zhu, Z.-Q.; Fu, W.; Liu, W.; Lei, J.; Lyu, S. Investigation of Hybrid-Magnet-Circuit Variable Flux Memory Machines with Different Hybrid Magnet Configurations. *IEEE Trans. Ind. Appl.* **2020**, *57*, 340–351. [CrossRef]
20. Baloch, N.; Kwon, B.-I. A pole changing vernier machine with consequent pole rotor. *Int. J. Appl. Electromagn. Mech.* **2019**, *59*, 931–941. [CrossRef]
21. Lee, S.-H.; Baloch, N.; Kwon, B.-I. Design and analysis of a double consequent pole changing vernier machine. *Int. J. Appl. Electromagn. Mech.* **2020**, *64*, 941–949. [CrossRef]
22. Baloch, N.; Atiq, S.; Kwon, B.-I. A Wound-Field Pole-Changing Vernier Machine for Electric Vehicles. *IEEE Access* **2020**, *8*, 91865–91875. [CrossRef]
23. Baloch, N.; Kwon, B.-I. A Distributed Winding Wound Field Pole-Changing Vernier Machine for Variable Speed Application. *IEEE Trans. Manag.* **2019**, *55*, 1–6. [CrossRef]
24. Maekawa, S.; Yuki, K.; Matsushita, M.; Nitta, I.; Hasegawa, Y.; Shiga, T.; Hosoito, T.; Nagai, K.; Kubota, H. Study of the Magnetization Method Suitable for Fractional-Slot Concentrated-Winding Variable Magnetomotive-Force Memory Motor. *IEEE Trans. Power Electron.* **2013**, *29*, 4877–4887. [CrossRef]
25. Asgar, M.; Afjei, E.; Behbahani, A.; Siadatan, A. A 12/8 double-stator switched reluctance motor for washing machine application. In Proceedings of the The 6th Power Electronics, Drive Systems & Technologies Conference (PEDSTC2015), Tehran, Iran, 3–4 February 2015; pp. 168–172. [CrossRef]
26. Li, F.; Chau, K.T.; Liu, C. Pole-Changing Flux-Weakening DC-Excited Dual-Memory Machines for Electric Vehicles. *IEEE Trans. Energy Convers.* **2015**, *31*, 27–36. [CrossRef]
27. Chung, S.-U.; Moon, S.-H.; Kim, D.-J.; Kim, J.-M. Development of a 20-Pole–24-Slot SPMSM with Consequent Pole Rotor for In-Wheel Direct Drive. *IEEE Trans. Ind. Electron.* **2015**, *63*, 302–309. [CrossRef]
28. Ibrahim, M.; Masisi, L.; Pillay, P. Design of Variable Flux Permanent-Magnet Machine for Reduced Inverter Rating. *IEEE Trans. Ind. Appl.* **2015**, *51*, 3666–3674. [CrossRef]
29. Limsuwan, N.; Kato, T.; Akatsu, K.; Lorenz, R.D. Design and Evaluation of a Variable-Flux Flux-Intensifying Interior Permanent-Magnet Machine. *IEEE Trans. Ind. Appl.* **2014**, *50*, 1015–1024. [CrossRef]
30. Hua, H.; Zhu, Z.Q.; Pride, A.; Deodhar, R.P.; Sasaki, T. A Novel Variable Flux Memory Machine with Series Hybrid Magnets. *IEEE Trans. Ind. Appl.* **2017**, *53*, 4396–4405. [CrossRef]
31. Jandaghi, B.; Dinavahi, V. Prototyping of Nonlinear Time-Stepped Finite Element Simulation for Linear Induction Machines on Parallel Reconfigurable Hardware. *IEEE Trans. Ind. Electron.* **2017**, *64*, 7711–7720. [CrossRef]
32. Yang, H.; Lin, H.; Zhu, Z.Q.; Wang, D.; Fang, S.; Huang, Y. A Variable-Flux Hybrid-PM Switched-Flux Memory Machine for EV/HEV Applications. *IEEE Trans. Ind. Appl.* **2016**, *52*, 2203–2214. [CrossRef]